

# High Pressure Tube Twisting for Producing Ultra Fine Grained Materials: A Review

Laszlo S. Toth<sup>1,2,\*</sup>, Cai Chen<sup>3</sup>, Arnaud Pougis<sup>4</sup>, Mandana Arzaghi<sup>5</sup>, Jean-Jacques Fundenberger<sup>1,2</sup>, Roxane Massion<sup>1,2</sup> and Satyam Suwas<sup>6</sup>

<sup>1</sup>Laboratoire d'Etude des Microstructures et de Mécanique des Matériaux (LEM3), UMR 7239, CNRS/Université de Lorraine, F-57045 Metz, France

<sup>2</sup>Laboratory of Excellence on Design of Alloy Metals for low-mAss Structures (DAMAS), Université de Lorraine, F-57045 Metz, France

<sup>3</sup>Sino-French Engineering School, Nanjing University of Science and Technology, No. 200 Xiaolingwei, Nanjing 210094, China

<sup>4</sup>Safran Aircraft Engines, Rond Point René Ravaut, 77550 Moissy-Cramayel, France

<sup>5</sup>ISAE-ENSMA, PPRIME UPR CNRS 3346, Poitiers, France

<sup>6</sup>Department of Materials Engineering Indian Institute of Science, Bangalore 560012, India

The High Pressure Tube Twisting (HPTT) process was first proposed in 2009 as an efficient new Severe Plastic Deformation (SPD) process. Since then it has been successfully applied on many different materials and the results have been reported in several publications and thesis works. The purpose of this overview is to present and evaluate the main results of the published papers and thesis works and also to present new contributions. Special attention is given to the strain gradient which appears in the tube wall for which a new empirical formula is presented. [doi:10.2320/matertrans.MF201910]

(Received January 30, 2019; Accepted March 18, 2019; Published June 25, 2019)

**Keywords:** high pressure tube twisting (HPTT), tube-high pressure shearing (t-HPS), severe plastic deformation (SPD), microstructure, texture, Al, Mg, Cu, IF steel

## 1. Introduction

The High Pressure Tube Twisting (HPTT) process was proposed in 2009 by Toth *et al.*<sup>1)</sup> This severe plastic deformation (SPD) technique is based on simple shear, like the ECAP<sup>2)</sup> and HPT<sup>3)</sup> processes. HPTT is a variant of HPT wherein instead of a disk, a thin-walled tube is subjected to very large shear strain levels in a single operation. Like HPT, HPTT is an efficient technique for producing ultra-fine grained (UFG) structured bulk materials with high strength.

The principle of HPTT is that the tube is perfectly constrained by two mandrels: an internal and external one; then the external mandrel is rotated, while the internal remains fixed. This operation induces a shear deformation in the tube wall, where the shear plane is normal to the radial direction and the shear direction is tangential to the surface of the tube. The shear stress is generated from the external torque by friction which is engendered by a large hydrostatic pressure. The latter is produced by an axial compression force, similar to HPT. The experimental procedure for performing HPTT is similar to HPT. Namely, after placing the tube within the die, first only the axial compression force is applied on the tube; the rotation operation follows after the compression stage is finished.

In the first conception of HPTT testing,<sup>1)</sup> the friction was generated by the elastic expansion of the internal mandrel, due to its axial compression, see Fig. 1. However, the level of hydrostatic pressure is limited for such testing, so a new design was made in 2012,<sup>4)</sup> where the axial force is applied directly on the tube wall (Fig. 2). Later Wang *et al.*<sup>5)</sup> presented another variant of HPTT where the axial force is transmitted to the tube via a small ring (Fig. 2(c)). They called the HPTT process differently; “tube high-pressure shearing, t-HPS”, but the principles of t-HPS are exactly the

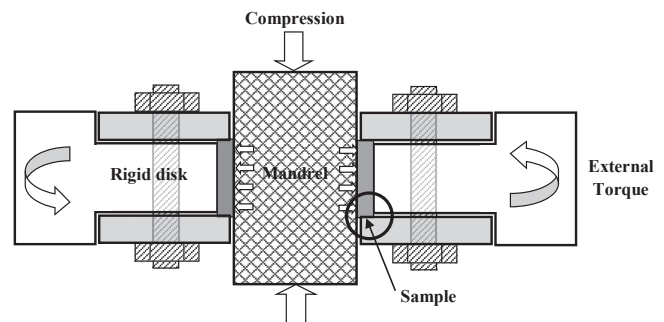


Fig. 1 The first setup for HPTT testing (2009,<sup>1)</sup> reproduced by permission).

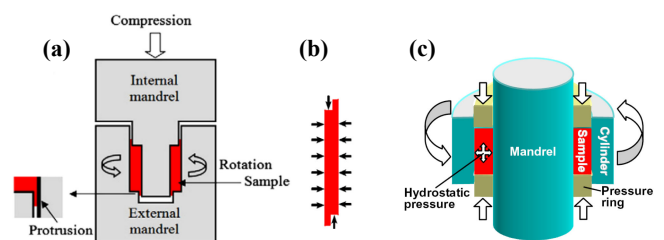


Fig. 2 The new versions of HPTT testing. (a): Schematic setup, (b): the compression stresses applied on the tube wall showing the protrusions.<sup>4)</sup> (c): A slightly modified version.<sup>5)</sup> (Figures reproduced by permissions.)

same as HPTT while t-HPS was proposed later than HPTT (in 2012 with respect to 2009). The t-HPS variant of HPTT was patented in China, see Fig. 3 for two patented versions of t-HPS.

The motivation for proposing the HPTT test was partly to remove the strain heterogeneity in the conventional HPT testing; it was expected that the shear strain would be homogeneous across the thin wall of the tube. It has been found, however, that there is a gradient in the shear strain across the thin wall.<sup>1,6)</sup> This phenomenon has been investigated experimentally<sup>1,4,6)</sup> and was also modeled

\*Corresponding author, E-mail: laszlo.toth@univ-lorraine.fr

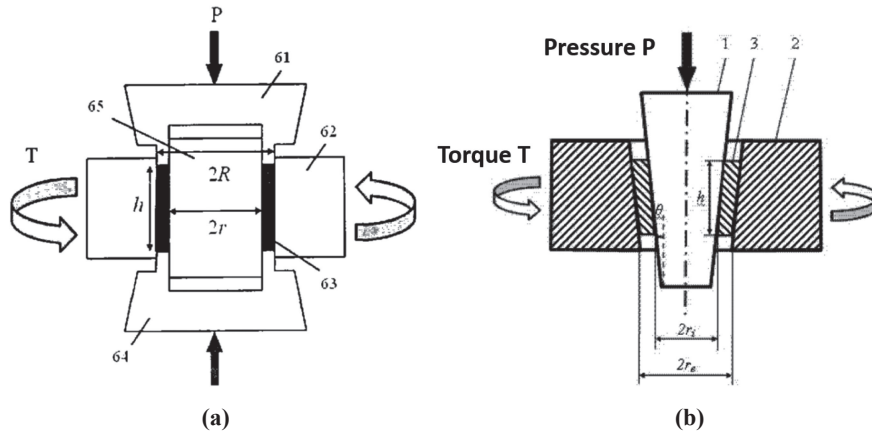


Fig. 3 Two Chinese patented versions of the HPTT testing. (a): CN 102189706 A; 2011.09.21. (b): CN 102500632; 2012.06.20.

theoretically.<sup>5,6)</sup> This point will be discussed also in the present paper and will be documented with the help of new experimental results.

The HPTT technique has been successfully applied on different materials (Al and its alloys,<sup>1,4,7,8)</sup> Mg,<sup>9)</sup> Cu,<sup>8,9)</sup> brass,<sup>9)</sup> Fe<sup>6,8)</sup>) and has been found to be very efficient in the grain refinement process leading to UFG structures. The present paper is an overview on the technical and theoretical aspects of the HPTT process and also on the evolution of textures and microstructures resulting from HPTT. We have examined the evolution strength by hardness test, microstructural features, like grain size, disorientation distribution using EBSD-IPF maps, and crystallographic textures by EBSD as well as X-ray diffraction.

## 2. Technical Characteristics of an HPTT Equipment

The first HPTT tests were carried out in the LEM3 laboratory of the University of Lorraine, Metz, France using an attachment developed in-house (Fig. 1) to a Zwick tensile machine and applying the torque by hand.<sup>8)</sup> Owing to the success in deforming commercially pure Al tube entirely within the tube wall, a new die was installed in an another Zwick compression-torsion equipment. In 2012 an independent equipment was built<sup>8)</sup> with the capacities necessary to deform various class of materials, see the photo in Fig. 4. The compression force is provided by a hydraulic system, capable to provide pressing force up to 750 kN. The torsion is applied by a motor through a redactor system, which can impart a maximum torque of 6000 Nm on the external mandrel. This capability of the machine allows to impose large deformations to the tubular metallic samples with approximate dimensions of 20/18 mm of external/internal diameters and a length of about 15 mm. The length limitation comes from the limited capacity of the internal mandrel in terms of torque. Namely, all external torque is spent in twisting the cross section of the internal mandrel, which can break if the load is too high. From the equality of the external torque and the internal one (produced by the mandrel), one obtains the following limitation on the ratio of length ( $L$ )/internal radius ( $r$ ) of the tube:<sup>4)</sup>

$$\frac{L}{r} \leq \frac{1}{4} \frac{\tau_0^m}{\tau_0^t}. \quad (1)$$

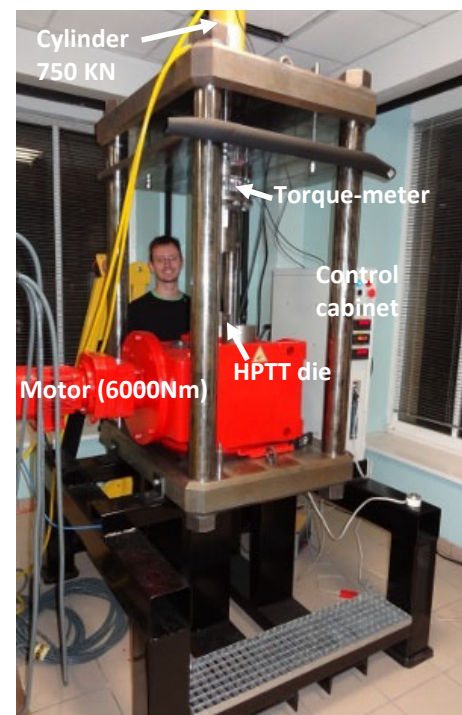


Fig. 4 The HPTT device built in Metz, France.<sup>8)</sup>

Here  $\tau_0^m$  is the shear flow stress of the mandrel and  $\tau_0^t$  is the maximum shear flow stress of the tube during deformation.

The mandrel material used in the Metz-equipment is a 45NCD16 steel, which has yield strength between 1800 and 2000 MPa after heat treatment. Figure 5 shows the limiting tube length/radius ratio for different materials for this kind of mandrel material. For example, for IF steel, a ratio  $L/r$  of 1.0 is needed to avoid breaking of the mandrel, while for Mg tubes, the tubes can be more than four times longer than their internal radius.

During the process, some protrusions are necessarily formed (indicated in Fig. 2(a)–(b)). They are important for fully constraining the tube, so that deformation instabilities are suppressed and cracking is eliminated thanks to the build-up of high hydrostatic stresses. The usual rotation speed of the external mandrel during processing is about 0.5°/s, and the tests are carried out at room temperature. The equipment is operated by computer control, the data are collected

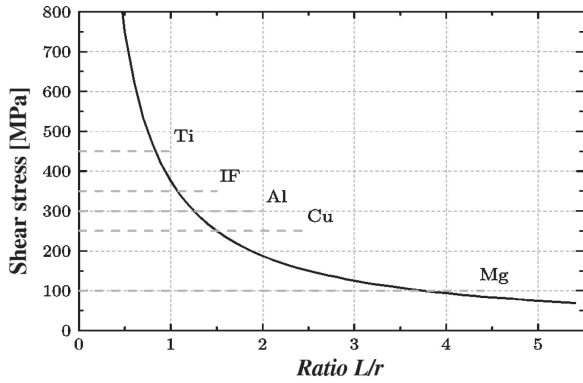


Fig. 5 The limitation on tube length of the HPTT process for different materials for a constant mandrel yield strength of 2000 MPa.

numerically (torque, twist angle, axial stress, axial strain). A small, but non-negligible axial strain develops during the testing so that the height of the tube is slightly decreasing during HPTT. This effect is due to the material outflow via the protrusions, and similar to the thickness reduction of the disk during HPT.

The principal advantage of the HPTT process is that it allows deforming tubes (though relatively short tubes), which are frequent in technical applications. It also produces relatively large samples with respect to the disks of HPT testing, which can be more easily examined by further mechanical testing and are readily suitable for microstructure characterization.

HPTT is a friction-driven SPD process, so special attention is needed to the contact surfaces between the anvils and the sample. It is necessary to sand-blast the anvil surfaces in contact with the sample to ensure good adherence, without slipping. The axial force has to be sufficiently large to produce the necessary hydrostatic stress which induces the frictional force. We have studied the hydrostatic stress distribution during HPTT with the help of finite element calculations using Abaqus.<sup>8)</sup> In the elastic regime, the hydrostatic stress is not uniform, however, when plastic deformation begins, the distribution of the hydrostatic stress becomes perfectly uniform, see Fig. 6(a). This is important for the homogeneity of strain along the axial direction of

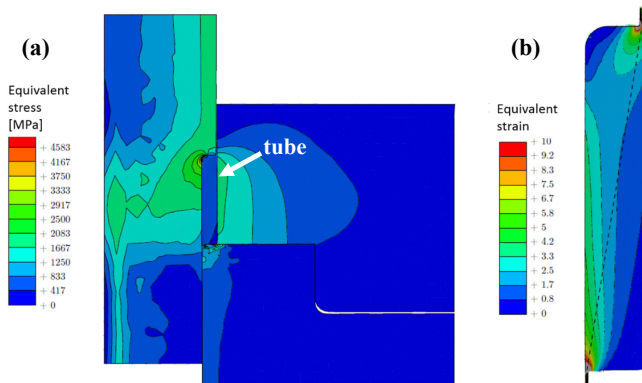


Fig. 6 (a): The distribution of the hydrostatic stress in the tube and the die during plastic deformation obtained by finite element simulation. (b): Predicted strain-map after a rotation of 30° of the tube (at about a nominal average shear strain of 4.0). Reproduction from Ref. 8.

the tube. While the hydrostatic stress is uniform during plastic deformation, the shear strain produced in the tube presents a gradient in the radial direction, see Fig. 6(b). This is due to the difference in the shear stress level between the internal and external surfaces of the tube, inherent to the test. This effect will be further elucidated in Section 4 below.

### 3. Average Stress and Strain in HPTT Testing

In analyzing the deformation processes, the calculation of stresses and strain is an important issue. In HPTT testing, there is a shear gradient across the tube wall. The integral of the local shear strain,  $\gamma(r)$ , is related to the total rotation angle  $\theta$  of the tube (which is the rotation of the external mandrel):<sup>1,6)</sup>

$$\theta = \int_a^b \frac{\gamma(r)}{r} dr \quad (2)$$

Here  $a$  and  $b$  are the internal and external radii of the tube, respectively. When  $\gamma(r)$  is replaced by the average shear strain  $\bar{\gamma}$ , the following relation can define the average shear strain:

$$\bar{\gamma} = \frac{\theta}{\ln(b/a)}. \quad (3)$$

Once the average shear strain is defined, an average shear stress  $\bar{\tau}$  can be also determined, using the equality of the external and internal plastic works,<sup>4)</sup> leading to:

$$\bar{\tau} = \frac{T \ln(b/a)}{(b^2 - a^2)\pi h}. \quad (4)$$

Here  $h$  is the height of the tube. Equations (3)–(4) permit the construction of a stress-strain curve. The torque ( $T$ ) versus rotation angle curves for different materials are shown in Fig. 7 for (for  $a = 7$ ,  $b = 8$  mm, and  $h = 7$  mm) together with the average strain-average stress curves. It is important to note that the above analysis neglects the torque that originates from the top and bottom surfaces of the tube in contact with the mandrels. It also neglects the friction forces between the mandrels and the protrusions. For this reason, the average shear stress is overestimated when the measured torque is used in eq. (4).

### 4. The Shear Gradient in the Tube Wall

During the HPTT deformation process, the stress state in the tube is represented by the following stress tensor  $\sigma$ :

$$\sigma = \begin{pmatrix} \sigma_{rr} & \tau & 0 \\ \tau & \sigma_{\theta\theta} & 0 \\ 0 & 0 & \sigma_{zz} \end{pmatrix}_{(r,\theta,z)} \quad (5)$$

It has been shown in Ref. 6) that the normal stress components are equal during plastic strain; they produce a hydrostatic stress state. By applying the equilibrium condition between the external torque  $T$  and the torque developed by the local shear stress, the following equation can be obtained for the shear stress variation within the tube:

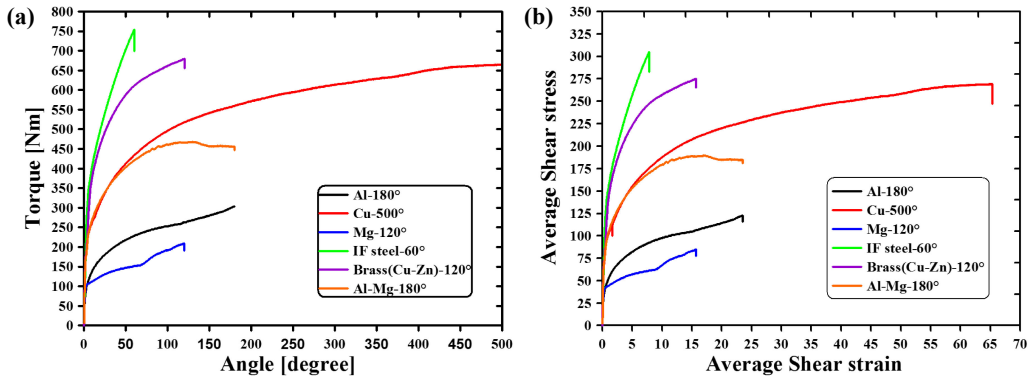


Fig. 7 (a): Torque vs. angle and (b): average shear stress vs. average shear strain for AA1050, Copper, Magnesium, IF steel, Brass and Al-Mg alloy deformed by HPTT.

$$\tau(r) = \frac{T}{2\pi hr^2} \quad (6)$$

As can be seen from eq. (6), the shear stress decreases as a function of the tube radius, which is contrary to the well-known situation of simple torsion and HPT, in which the shear stress is increasing as a function of the radius. It has been shown in Refs. 5, 6) that by adopting a suitable strain hardening curve, eq. (6) can be used to express the shear strain as a function of the radius. As large strain hardening is of interest in SPD, the strain hardening stages III and IV were used in Ref. 6) in the forms:

$$\tau_{III} = K\gamma^n \text{ (Stage III) and } \tau_{IV} = A + B\gamma \text{ (Stage IV)}. \quad (7a,b)$$

By substituting eqs. (7) into eq. (6), the following strain gradient equations were obtained for the shear strain:<sup>6)</sup>

$$\gamma(r) = \left( \frac{T}{2\pi hKr^2} \right)^{1/n} \text{ in Stage III, and} \quad (8a)$$

$$\gamma(r) = \frac{T}{2\pi hBr^2} - \frac{A}{B} \text{ in Stage IV.} \quad (8b)$$

The above analytic strain gradient equations were compared to the experiments that were carried out on IF steel.<sup>6)</sup> Experimentally, the shear strain was measured from the inclination axes of the grains with respect to the simple shear reference system. Namely, under simple shear, an initial spherical grain elongates into an ellipsoidal form. The imposed shear strain can be obtained from the orientation  $\alpha$  of the main axis of the ellipse with respect to the shear direction, as shown in Fig. 8. The following relation can be used for this purpose:<sup>12)</sup>

$$\gamma = \frac{2}{\tan(2\alpha)}. \quad (9)$$

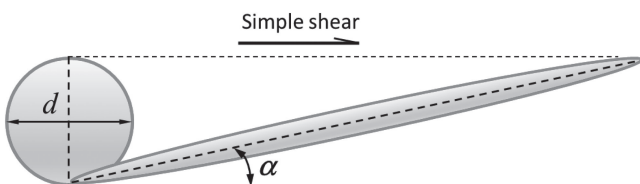


Fig. 8 Schematic illustration of a grain shape deformation obtained by simple shear.

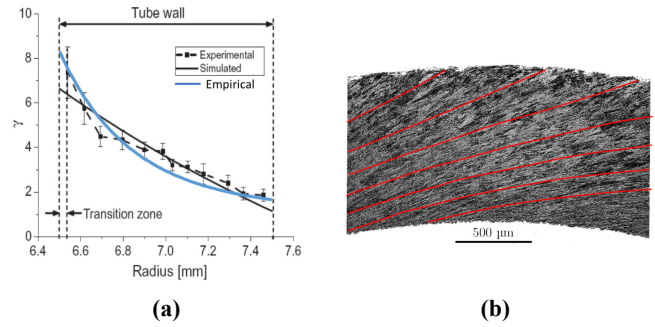


Fig. 9 (a): Measured and simulated strain gradient within the tube wall in a 30° HPTT deformed IF steel tube (from Ref. 6). The blue curve is obtained from the empirical equation (eq. (14)) with  $n = 2$ ,  $m = 20$ . (b): Micrograph of the IF steel tube showing the spirals corresponding to eq. (11) (from Ref. 8).

From optical metallographic images,  $\alpha$  can be measured. The measured and predicted shear strain gradients are shown for IF steel in Fig. 9(a) (from Ref. 6)).

It was discussed in Ref. 13) how an initially radial line within the tube wall acquires a kind of spiral due to the large shear. The authors used the Stage III type hardening expressed by the Swift-type hardening rule (eq. (7a)) for this purpose which provides the strain gradient within the wall in a similar way as presented above. Then the so-obtained strain gradient function can be substituted into eq. (2), from which the equation of the spiral can be obtained in polar coordinates:  $r$  and  $\phi$ .

However, Stage III does not generally appear within the tube because even for a rotation angle as small as 30°, the lowest strain in the tube is already in Stage IV. This was clearly observed in the case of HPTT of the IF steel sample (see Fig. 9(a)). Therefore, for rotation angles larger than 30°, it is more justified to use the Stage IV constitutive law for strain hardening. For Stage IV, the equations for the spirals can be obtained in the same way as was done by Li *et al.*<sup>13)</sup> First we obtain the shear strain as a function of the radial position by expressing  $T$  as a function of the Stage IV parameters in eq. (8b):

$$\gamma(r) = \frac{2}{Br^2} \left( B\theta - A \ln \frac{a}{b} \right) \left( \frac{1}{a^2} - \frac{1}{b^2} \right)^{-1} - \frac{A}{B}. \quad (10)$$

Then, by inserting this function into eq. (2) and integrating we obtain the equation that describes the spiral:

$$\phi = \left( \theta - \frac{A}{B} \ln \frac{a}{b} \right) \left( \frac{1}{a^2} - \frac{1}{b^2} \right)^{-1} \left( \frac{1}{a^2} - \frac{1}{r^2} \right) - \frac{A}{B} \ln \frac{r}{a}. \quad (11)$$

Using the same parameters as for Fig. 9(a), the spirals were superimposed in Fig. 9(b) on the micrograph of IF steel taken by scanning electron microscope.<sup>8)</sup> (The parameters were:  $\theta = 30^\circ$ ,  $a = 7$  mm,  $b = 8$  mm,  $A = 250.5$  MPa and  $B = 16.2$  MPa.<sup>6)</sup> As can be seen, the spirals are tangent to the axes of the elongated grains which justifies the use of eq. (9) for estimating the local shear strain in HPTT.

Another example for strain gradient, obtained for HPTT of Al, is presented in Figs. 10–11 as a function of increasing rotation angle of the tube.<sup>9)</sup> As can be seen from these figures, the strain gradient persists, even at very large strains. This result indicates that there must be continuous strain hardening, even at extreme large strains, because strain hardening is needed for the existence of strain gradient. Indeed, the measured torque and the average stress generally increases continuously as a function of twisting, see in Fig. 7 (except for the Al–Mg alloy which arrives to saturation of the torque at about a rotation angle of  $100^\circ$ ).

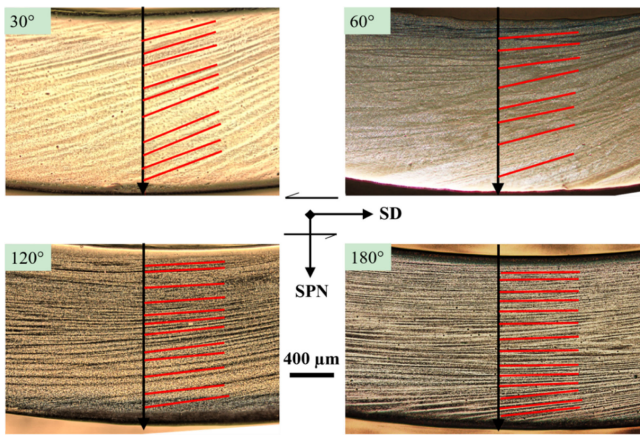


Fig. 10 Optical micrographs of deformed aluminum tube at different rotation angles showing the inclination of the deformation traces (red segments) with respect to the radial lines (black arrows) (from Ref. 9). SD: shear direction, SPN: shear plane normal.

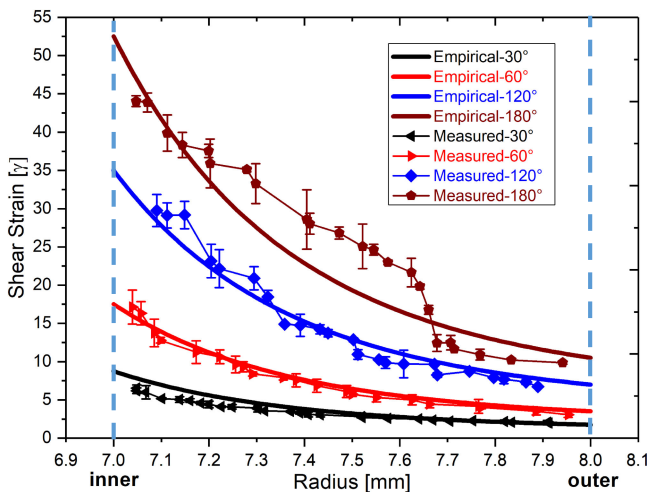


Fig. 11 Shear strain gradient within the tube wall in the radial direction in commercially pure aluminum after HPTT of different rotation angles. The empirical fit was obtained using eq. (14).

An interesting observation from Fig. 11 is that the ratio of the maximum and minimum shear strains, measured at the internal and external radii, respectively, is nearly constant, independently of the strain level:

$$\gamma_a/\gamma_b \cong \rho. \quad (12)$$

For Fig. 11, this ratio is about 5. Using this observation, an empirical fitting is proposed in the following to describe the strain gradient. A simple function is constructed that can fit satisfactorily the local shear strain as a function of the local radius within the tube wall:

$$\gamma(r) = \frac{C}{r^n} + \frac{D}{r^m}. \quad (13)$$

Here  $C$ ,  $D$ ,  $n$  and  $m$  are constants. Assuming  $n$  and  $m$ , both  $C$  and  $D$  can be determined using eqs. (2) and (5). We obtain the following:

$$\gamma(r) = \theta p \left( \frac{1}{r^n} - \frac{g}{r^m} \right), \quad (14)$$

where  $p$  and  $g$  are defined by  $\rho$ , the  $n$  and  $m$  exponents, and by the geometry parameters  $a$ , and  $b$ :

$$p = \left[ g \left( \frac{1}{nb^n} - \frac{1}{na^n} \right) - \left( \frac{1}{mb^m} - \frac{1}{ma^m} \right) \right]^{-1},$$

$$g = \left( \frac{1}{a^m} - \frac{\rho}{b^m} \right) \cdot \left( \frac{1}{a^n} - \frac{\rho}{b^n} \right)^{-1}. \quad (15a,b)$$

For the gradients shown in Fig. 11, the  $n$  and  $m$  values were identified as  $n = 2$  and  $m = 20$  ( $\rho = 5$ ,  $a = 7$  mm and  $b = 8$  mm). The corresponding empirical curves are also plotted in Fig. 11 for HPTT of Al. The same empirical function was used also for the IF steel HPTT experiment; the fit is shown in Fig. 9 with blue line. As can be seen, there is relatively good agreement between the measured and empirical curves for different materials. Therefore, the empirical relation can be used for obtaining a good estimation of the local shear strain value at any point within the tube wall. Concerning the parameters employed in this empirical formula;  $n$ ,  $m$  and  $\rho$ , they correspond to the given geometry ( $a = 7$  mm et  $b = 8$  mm), and might depend on the material. New experiments are needed to find out how these parameters change for another geometry and other materials.

Using the proposed empirical strain gradient equation (eq. (14)) in eq. (2) (by replacing  $\theta$  with  $\phi$  and  $b$  with  $r$ ), we obtain the following equation for the spiral:

$$\phi = \theta p \left[ g \left( \frac{1}{nr^n} - \frac{1}{na^n} \right) - \left( \frac{1}{mr^m} - \frac{1}{ma^m} \right) \right]. \quad (16)$$

(Here  $\theta$  is the applied external rotation angle.) An application of this equation is shown in Fig. 12 for two turns ( $\theta = 720^\circ$ ) with  $\rho = 5$  and for  $a = 7$  mm,  $b = 8$  mm using the same  $n$  and  $m$  parameters as for Fig. 11. This equation is useful to examine the geometry of the layers when HPTT is used for architecturing the deformed metal, see in Section 11.

The origin of the strain gradient within the tube wall is the gradient in stress. Using eq. (6) we can write:

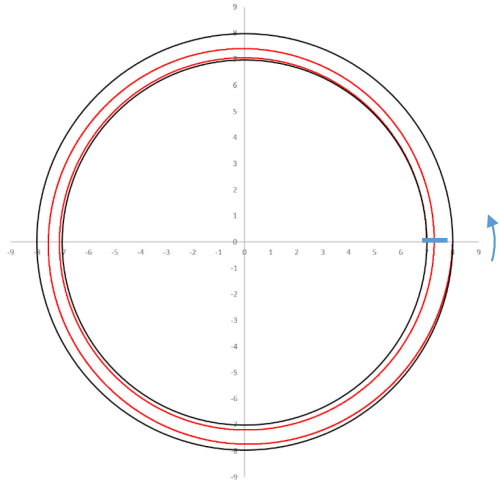


Fig. 12 The spiral formed from an initially radial segment (in blue) during two turns in HPTT (red line) plotted from eq. (16) for internal and external radius of 7 mm and 8 mm, respectively.

$$\frac{\tau_a}{\tau_b} = \left(\frac{b}{a}\right)^2. \quad (17)$$

According to this formula, the stress level has to be always higher in the inside region with respect to the outside one, by a constant proportion during the whole testing. Due to this, not only the stress but also the strain levels are higher in the inside region. The flow stress of the material must follow this variation, which is possible, due to strain hardening. Initially, when the flow stress is constant, plastic deformation begins in the inside zone and the plastic zone progressively extends to the whole volume while strain hardening is always higher near the interior tube wall. This is why the strain is also higher in the inside part. As can be seen from the experimental results, the deformation increases everywhere in the wall. However, the rate of strain hardening is decreasing as strain increases, so the difference in stress level provided by strain hardening can become insufficient at large strains, so that eq. (17) is not satisfied. In fact, this effect is questioning in the possibility to reach the steady state in the outside zone. Indeed, when the steady state is reached, the flow stress of the material is constant which is not compatible with the condition imposed by eq. (17). This reasoning assumes that the flow stress is independent from the strain rate. However, it has been shown that strain rate sensitivity increases very significantly at large strains<sup>12)</sup> and in UFG materials.<sup>13)</sup> The effect of strain rate sensitivity is that the flow stress is higher for higher strain rate, so a non-uniform stress state can exist in the steady state. Indeed, the strain rate is about 5 times higher in the internal wall of the tube, thus the strain rate is also 5 times higher;  $\rho = 5$  in the experiments on aluminum (Fig. 11). Knowing the  $\rho$  value and the tube wall geometry, one can estimate the value of the strain rate sensitivity index.

We write the constitutive equation for strain rate sensitivity:

$$\tau = \tau_{ref} \cdot \left(\frac{\dot{\gamma}}{\dot{\gamma}_{ref}}\right)^m, \quad (18)$$

where  $m$  is the strain rate sensitivity index and ref. means reference value. The flow stress can be equal to the reference

value, or higher, or smaller. Using this relation for the internal and external radial positions, we can write:

$$\frac{\tau_a}{\tau_b} = \left(\frac{\dot{\gamma}_a}{\dot{\gamma}_b}\right)^m = \rho^m. \quad (19)$$

From eqs. (17)–(19) we obtain a formula for the value of the strain rate sensitivity:

$$m = [2 \ln(b/a)] / \ln \rho. \quad (20)$$

In most of the presented experiments the tube dimensions were:  $a = 7$  mm and  $b = 8$  mm, so we obtain for  $\rho = 5$ :  $m = 0.19$ . This seems to be a high value for room temperature deformation of metals, nevertheless, strain rate sensitivity can contribute significantly for maintaining the plastic flow in the whole tube. An experimental example was provided in Ref. 8) where a copper tube was twisted by  $500^\circ$  (average strain: shear of 108). The steady state was reached in the whole wall thickness with an average grain size of 240 nm and 270 nm in the internal and outside zones, respectively. The slightly larger grain size in the outside region can be explained with the effect of strain rate in the DRX process which is expected to be higher for the lower strain rate case in the outside region of the tube.

## 5. HPTT Testing of Commercially Pure Al

### 5.1 Microstructures at relatively low strains

Commercially pure (CP) Al AA1050 material was twisted to  $30^\circ$ , which corresponds to an average shear strain of 3.8. Figure 13 displays the inverse pole figure maps obtained by EBSD, as well as the disorientation angle distributions at three locations in the tube wall: outer, mid and inner positions.<sup>9)</sup> The color code in the IPF maps corresponds to the orientation of the axis of the tube (AD in the figure). Note that in this work all EBSD and texture measurements were analyzed with the ATOM and JTEX software.<sup>14,15)</sup>

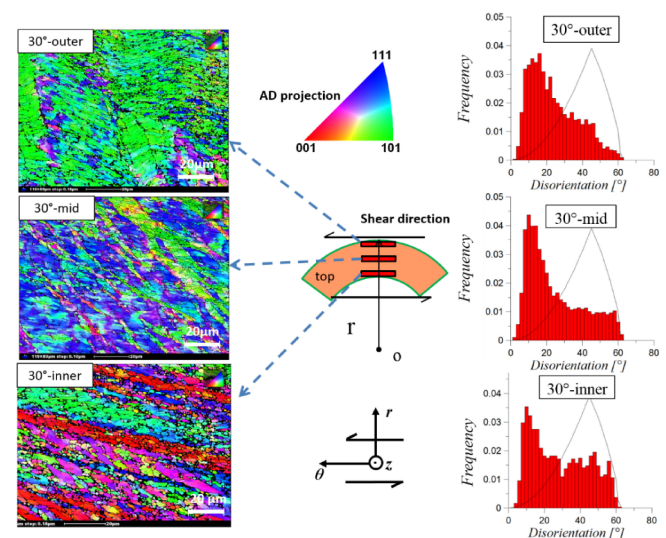


Fig. 13 Typical IPF orientation maps together with disorientation angle distributions in AA1050 for relatively low HPTT strain ( $30^\circ$  rotation; average shear is 3.8) at different regions of the tube section, named outer, mid and inner positions. The color code corresponds to the axial direction (AD) of the tube.

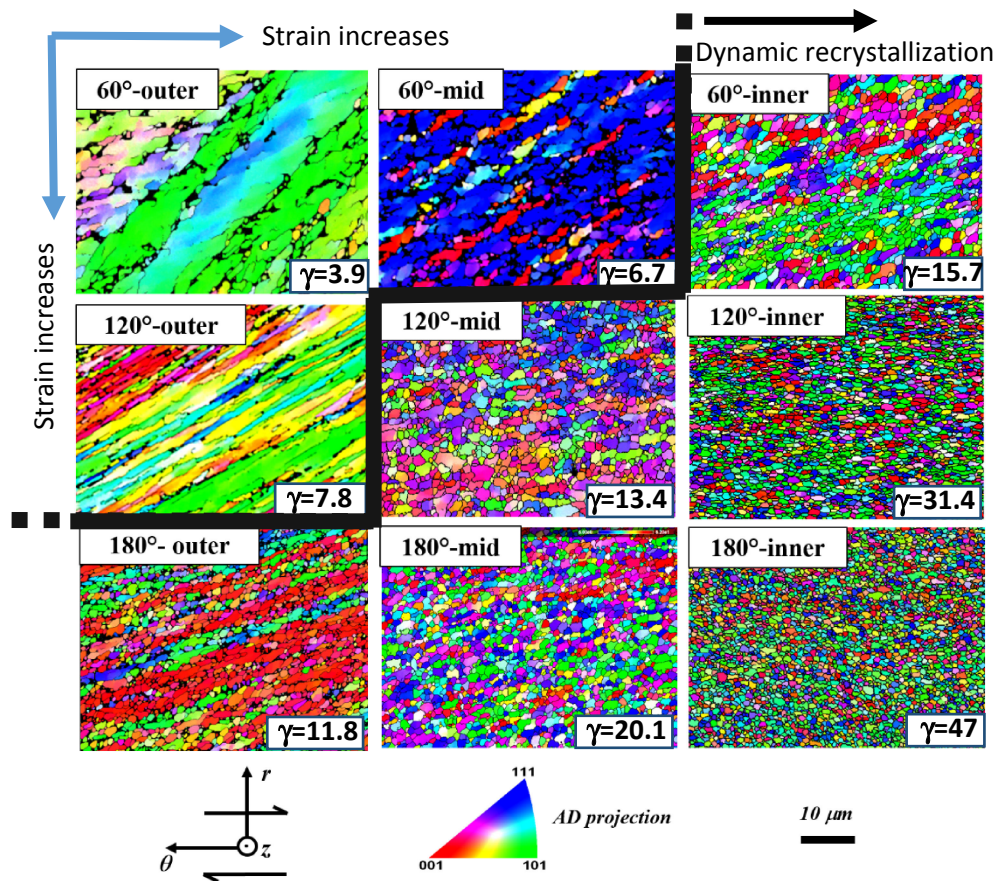


Fig. 14 IPF orientation maps of 60°, 120°, 180° twisted AA1050 samples at inner, middle and outer regions. The indicated shear values are the local estimated strains using Fig. 11. Black thick line indicates the limit of occurrence of dynamic recrystallization. The indicated shear strain values were obtained from the empirical relation (eq. (14)) using  $n = 2$ ,  $m = 20$ .

As can be seen, the microstructure is much more refined in the inner region, where the estimated shear strain is about 5. In the outer position, one can even distinguish the initial grains; the grain refinement is restricted to the grain interiors. The grains are much more elongated in the inside part, which is a sign of larger strain. Nevertheless, at local positions, the grain elongation does not necessarily follow the shear strain, which is a consequence of grain subdivision and also the local nature of the microstructure.

The microstructure heterogeneity leads to significant differences in the disorientation angle distributions, see Fig. 13. It is important to emphasize here that Fig. 13 shows the next-neighbor grain-to-grain disorientation distribution, not the usual pixel-to-pixel disorientations. Such grain-to-grain disorientation analysis was first introduced by Toth *et al.*,<sup>16</sup> which has more physical meaning from polycrystal plasticity viewpoint compared to the usually presented pixel-to-pixel disorientations. In this method, the grains are first identified by 5° tolerance angle, then the average orientation of the grain is calculated. Finally, the disorientations are obtained between these adjacent average orientations. The main feature of the distributions is a progressive evolution from a single peak to double peaks. The first peak can be attributed to the subdivision in grain interiors while the second one is due to the progressive lattice rotation of grains at large strains.<sup>4,16</sup>

## 5.2 Microstructures at large strains in commercially pure Al

Figure 14 shows typical orientation maps of AA1050 twisted by 60°, 120°, and 180° in HPTT,<sup>9</sup> with corresponding average shear strains of 8, 16 and 24, respectively. The maps shown were measured in the cross section of the tube (plane normal: ND). The local shear strain values are indicated in each map, using the strain estimates from Fig. 11. Even at these large strains, the effect of the strain gradient is clearly visible in the microstructures. Up to about shear strain of 12, the grains appear elongated and parallel to each other. These kinds of microstructures match those observed in CP Al deformed by a few ECAP passes<sup>17–19</sup> and also those obtained at low twist angles in HPT.<sup>20,21</sup> The microstructure is radically different at larger shear strains; in the middle and inner regions of the 120° and 180° twisted samples. Beyond the shear strain of 12, grain elongation is very much reduced, neighboring grains have very different orientations, and the grain size is very small. At these large strains, the microstructures show clearly the fingerprints of dynamic recrystallization which reduces the elongation of the grains that is expected from the shear strain. A nearly equiaxed grain structure develops which must be the consequence of deformation induced grain boundary migration, that is, a process of continuous dynamic recrystallization (CDRX).

Figure 15 shows the average grain size as a function of the local shear strain, obtained from the microstructures of

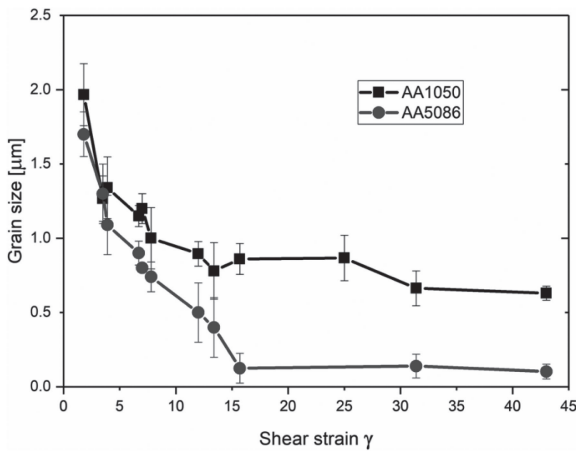


Fig. 15 Grain size evolution in AA1050 and AA5086 aluminum tubes as a function of shear strain at the internal surface of the tube.

Figs. 13–14. Note that the initial average grain size was about 300  $\mu\text{m}$ , then it decreased rapidly down to about 2  $\mu\text{m}$  after a shear strain of 2. Starting from about shear of 20, the grain size gets stabilized at around 0.65  $\mu\text{m}$ , although the tendency curve does not yet show an asymptote. This value is near to that obtained in HPT,<sup>3,20</sup> which is natural since the strain mode is practically the same for HPTT and HPT; monotonic simple shear with high hydrostatic pressure. However, the minimum grain size is much larger in ECAP; it was reported to be about 1.2  $\mu\text{m}$ .<sup>18,19</sup> The difference can be attributed to the large hydrostatic stress in HPT and HPTT which slows down the dislocation annihilation processes, including the geometrically necessary dislocations which are responsible for the grain fragmentation process.

As mentioned above, with increasing strain level, usually two peaks appear in the disorientations distribution figures: one is at the low disorientation (less than  $\sim 20^\circ$ ) and the other is at high disorientations (more than  $\sim 40^\circ$ ). The peak appearing at low disorientation angles can be attributed to the formation of subgrain boundaries, while the increasing fraction of HAGB finds its origin partly in the formation of new grains as well as in the texture evolution. Indeed, texture evolution means rotation of individual grains near to ideal

positions which may involve very large rotations with respect to their neighbor’s rotation. An example of the evolution of the disorientation distribution is shown in Fig. 16 for the case of CP Al deformed by HPTT up to a shear strain of 24 (see Ref. 22)). A monotonic evolution of the distribution can be seen in Fig. 16(a), with progressive increase of the HAGB fraction. This is what plotted in Fig. 16(b): the fraction of HAGBs as a function of shear strain. Such a ‘master’ curve has been used to estimate the amount of shear strain in a shear process where the amount of shear strain was not known by other means<sup>22</sup>).

### 6. HPTT of AA5086 Al Alloy

Al alloys are preferred in applications when weight is an issue. We have examined the microstructure of tubular AA5086 Al alloy after subjecting it to HPTT, and compared to commercially pure Al.<sup>9</sup>) The experiments were carried out on tubes at room temperature, for 30°, 60°, 120° and 180° rotations. The internal and external diameters were the same as for the CP Al; 7 and 8 mm, respectively.

The evolution of the disorientation distributions and the EBSD maps are shown in Fig. 17. The initial state was composed of grains with moderate grain size (about 50  $\mu\text{m}$  in diameter) and the next neighbor disorientation distribution was nearly random (Fig. 17(a)). At shear strains of 3.4 and 6.7 the grains were subdivided and elongated (Fig. 17(b)), especially at a shear of 6.7. At the same time the disorientation distribution had a large peak near 12°. Further straining led to new features in the microstructure; at a shear of 13.4 the grains were clearly elongated, but at a shear of 20.1, the elongation was reduced. At the same time, there was very significant evolution in the disorientation distribution; a random distribution was approached with differences that can certainly be attributed to the deformation texture that must be present in the material (see the textures in the next section).

The grain fragmentation was much more relevant in the AA5086 alloy with respect to the CP Al; Fig. 15 displays the average grain size evolution (based on equivalent circle diameter and counted in number fraction) in comparison to

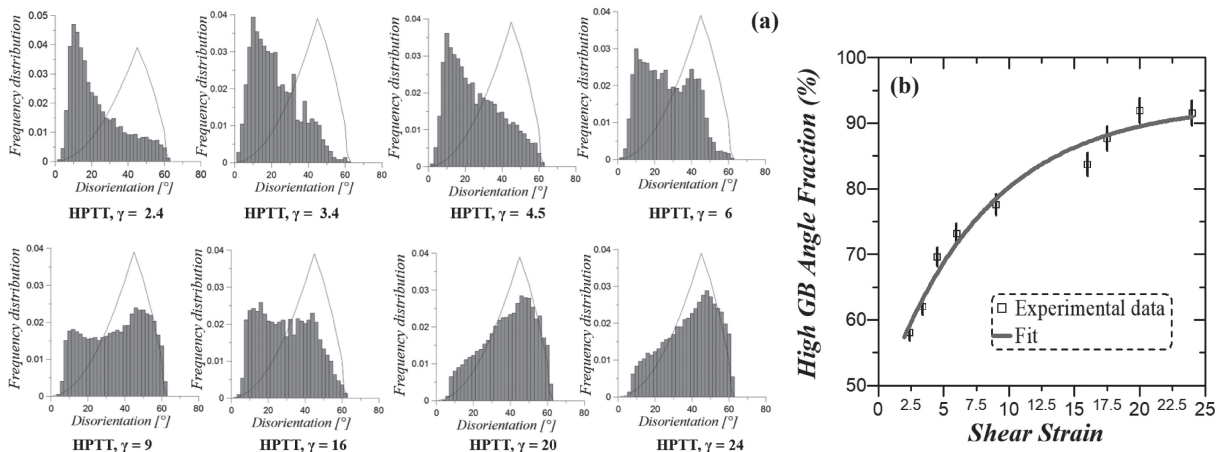


Fig. 16 (a) Disorientation evolution in Al at increasing shear strains. (b) Fraction of high grain boundaries angle versus shear strain<sup>22</sup>) (reproduced by permission).

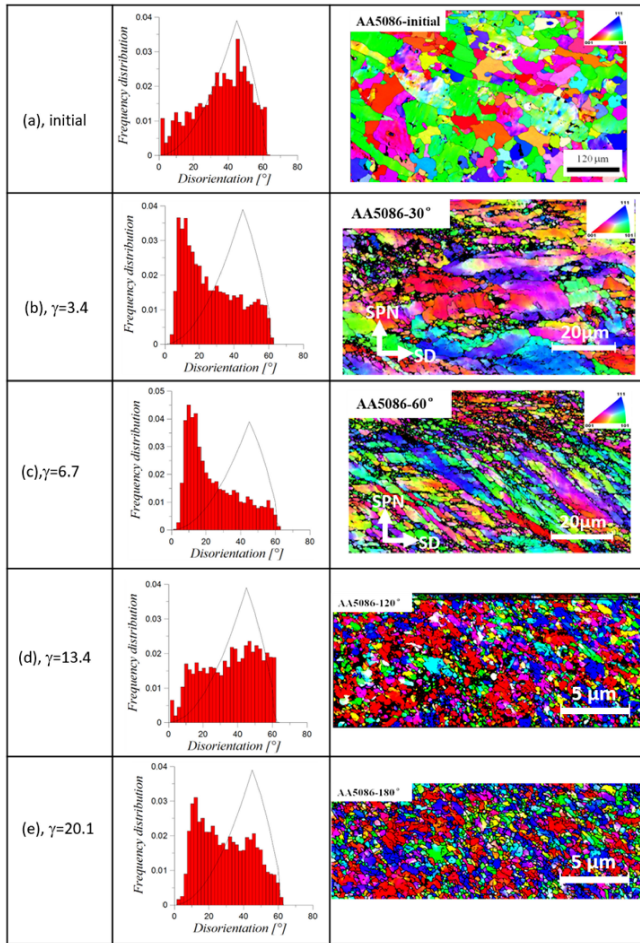


Fig. 17 Next-neighbor disorientation distributions and IPF maps observed in AA5086 Al alloy deformed by HPTT to different rotation angles in the middle part of the tube-wall. (a): Initial microstructure, (b), (c), (d), (e): after 30°, 60°, 120° and 180° twisting, respectively.

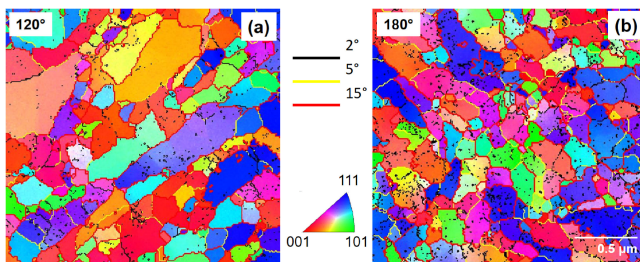


Fig. 18 IPF orientation maps obtained by TKD for the AA5086 alloy HPTT-twisted to 120° (a) and 180° (b).<sup>23)</sup>

CP Al as a function of strain. The grain size went down as low as 100 nm in the alloy. This is so small that conventional EBSD is not easily applicable for examining this highly deformed material; so the new TKD technique<sup>21)</sup> was applied for these two higher strained samples. Figure 18 shows the microstructure at 120° and 180° twisting angles obtained by TKD. As can be seen, there are more elongated grains at the lower strain (Fig. 18(a)) compared to the higher one (Fig. 18(b)). It is also apparent from these orientation maps that the equiaxed grains are products of a subdivision process of the elongated ones with the help of new grain boundaries that are nearly perpendicular to the direction of the grain elongation.

## 7. Texture Development in HPTT Deformed CP Al and AA5086 Alloy

Texture evolution is due to the orientation change of the grains of the polycrystal which depends on the individual grain orientations. It also depends on the deformation mechanisms that produce the plastic deformation of the polycrystal. Finally, at large strains grain orientations stop rotating, arriving to the so-called ideal orientations. For each deformation mode, there exists a characteristic ideal texture. Texture can be conveniently represented in pole figures; in this work we present them in  $\{111\}$  pole figures, suitable for fcc crystal structures. As the main deformation mode in HPTT is simple shear, we compare the measured textures with the ideal orientations of simple shear textures; they are depicted in Fig. 19(a). Textures are statistical by their nature, so large number of grain orientations are needed to measure them. The most suitable technique for measuring textures is XRD, which was applied in the present case.

Figure 19(b) shows the texture evolution for both CP Al and for the AA5086 alloy, for large HPTT strains, up to a shear strain of 44. All textures were measured on the internal surface of the tube-wall and the indicated shear strain values are all local strains, obtained by eq. (14). The textures are presented by projecting the  $\langle 111 \rangle$  directions on the sample plane with normal axis parallel to the axis of the tube. All measured textures confirmed the existence of simple shear textures, as expected. For all cases, the main deformation texture component was the C, which is defined by  $\{100\} \parallel \text{SPN}$  and  $\langle 011 \rangle \parallel \text{SD}$  (SPN: shear plane normal, SD: shear direction), it is basically a rotated cube orientation (rotation around the shear plane normal).<sup>4,7)</sup> Other relevant components that are well visible in the textures of Fig. 19 are: the  $A1^*/A2^* \{11\bar{1}\}\langle 2\bar{1}1 \rangle$  and  $A/\bar{A} \{11\bar{1}\}\langle 1\bar{1}0 \rangle$ .

## 8. HPTT of Pure Mg

The initial microstructure of the Mg sample was characterized by equiaxed grains with a grain size of about 50  $\mu\text{m}$  and a weak texture. The evolution of the microstructure was studied first right after the compression stage of the HPTT test. Figure 20(a) shows the IPF map of the as-compressed pure Mg sample without any rotation by HPTT process.<sup>9)</sup> The imposed pressure was 1 GPa along the axis direction of the tube, and the color code in the triangle represents the ED direction (axis of the tube) in the crystal system.

As can be seen in Fig. 20(a)–(b), large number of twins were generated only by the initial compression stage, which is a relatively small deformation. (During this compression stage the protrusions are formed requiring a small strain only.) Both contraction and extension twins were detected in Fig. 20(a)–(b); they were traced with red lines in Fig. 20(b). Two types of compression twins were detected: the type of 60.3° by rotation around  $\langle 1\bar{1}00 \rangle$ , and the type with 57.3° rotation around  $\langle 11\bar{2}0 \rangle$ . Extension twins were seen in the highest volume fraction among the three type twins; they were characterized by 86° rotation around  $\langle 11\bar{2}0 \rangle$ . Figure 20(c) displays the next-grain-neighbor disorientation angle distribution, which clearly shows that the main twin

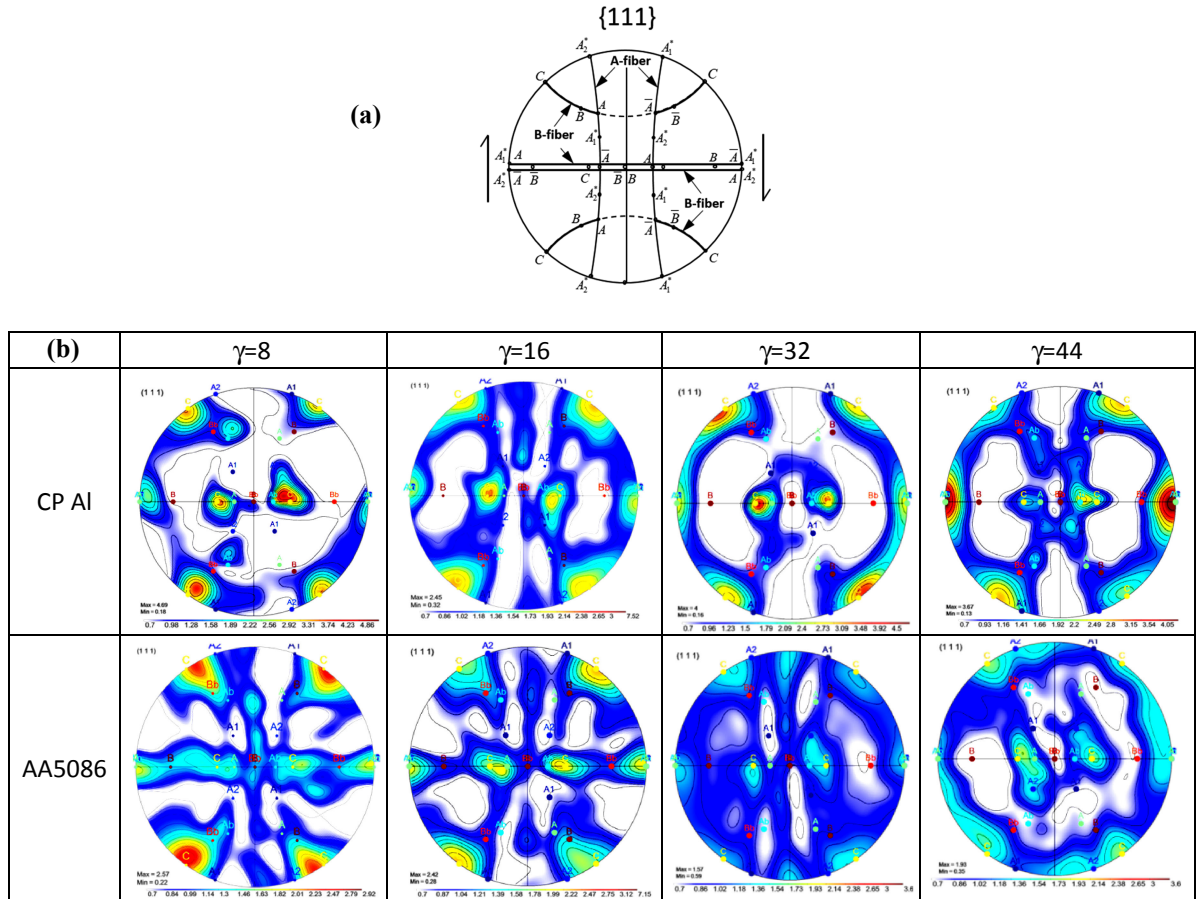


Fig. 19 Texture evolution of CP Al and AA5086 Al alloy during large HPTT deformation presented in {111} pole figures. (a): The ideal orientations of fcc simple shear textures. (b): Texture evolution, obtained by X-ray measurements on the internal surfaces of the tubes.

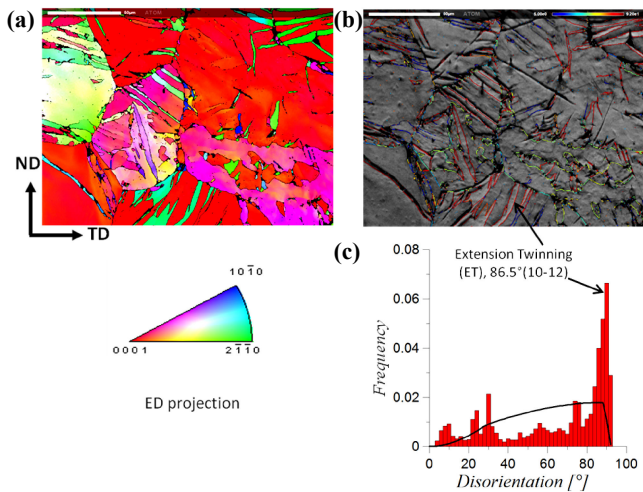


Fig. 20 Microstructure of the only compressed Mg tube. (a): IPF map. (b): In band contrast map with twins identified, (c) disorientation angle distribution. The black line in (c) traces the random disorientation angle distribution.

component in the as-compressed pure Mg corresponded to extension twins.

Figure 21 shows the microstructure in EBSD IPF maps for the 15° twisted tube in the SD-SPN plane as a function of the position within the tube. The imposed average shear strain was about 2 for 15° twisting. However, as mentioned before, a strain gradient existed in the wall thickness, so the local

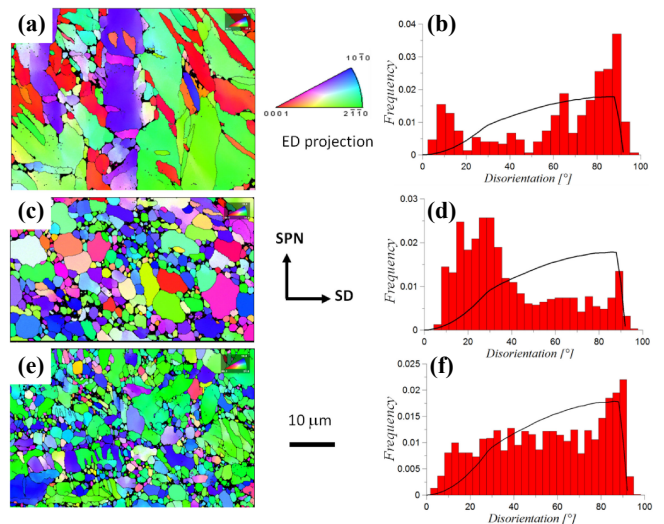


Fig. 21 Microstructures represented in IPF maps for the 15° twisted Mg tube sample in different regions (a) outer ( $\gamma \cong 1.0$ ); (c) middle ( $\gamma \cong 2.8$ ); (e) inner ( $\gamma \cong 3.9$ ). The corresponding disorientation distributions are shown in (b), (d), and (f). The color code corresponds to the orientation of the SPN axis with respect to the crystal reference system.

shear strain within the inner region was larger than in the outer region. An application of the empirical formula (eqs. (14) and (15)) with  $a = 7$  mm,  $b = 8$  mm and  $s = 6.57$  leads to the following strain estimates:  $\gamma \cong 3.9, 2.8, 1.0$  at the inner, middle and outer regions, respectively. In the

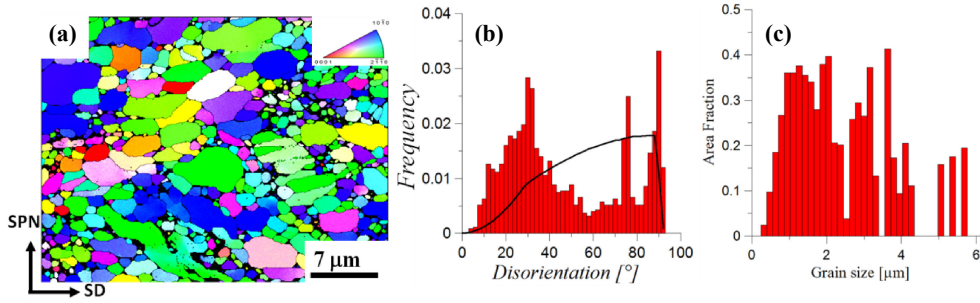


Fig. 22 Mid region of the 120° twisted Mg sample ( $\gamma \cong 8$ ) in (a) IPF map; (b) disorientation distribution; (c) grain size distribution in area-fraction.

outer part, large number of twins are visible in the IPF map (Fig. 21(a)); they also produced a large peak in the disorientation distribution at 86° (Fig. 21(b)). In the middle region, an advanced state of grain fragmentation became evident (Fig. 21(c)). A duplex structure appeared with large grains surrounded by small ones. The disorientation distribution changed radically for angles less than 40°; it shows a large peak in Fig. 21(d). This is due to the grain fragmentation process. The peak intensity for extension twins was reduced more than twice. This does not mean, however, that some twins disappeared. Indeed, due to the large number of small grains that were formed at lower angles, the relative intensity the large-angle peak was necessarily reduced. In the internal region of the tube-wall, where the strain is the largest ( $\gamma \cong 3.9$ ), the IPF map looks similar to the medium region, however, there is a radical change in the disorientation distribution: the large peak at lower angles disappeared and the random distribution is approached. The average grain size decreased from the initial 50  $\mu\text{m}$  to 6  $\mu\text{m}$  at the outer region, to 1.3  $\mu\text{m}$  in the middle part, and to 1.1  $\mu\text{m}$  in the inner region (number-weighted averages).

Figure 22 shows the microstructure of the 120° twisted Mg sample in its middle region, where the shear strain is about 8. The microstructure is similar to the lower strain cases (see Fig. 21) with a bimodal structure. The disorientation angle distribution is also “bimodal” as it displays a large peak at lower angles and two others at large angles. The peak at 86° is due to the extension twins which are still present at this extreme large strain (Fig. 22(b)). The area-fraction grain size distribution is clearly bimodal (Fig. 22(c)) with a population of grains larger than 2.5  $\mu\text{m}$ . The average grain size in number fraction is about 900 nm, which is about the same as in ECAP processed pure Mg at room temperature (Biswas *et al.*<sup>24</sup>).

The evolution of the crystallographic texture in Mg due to HPTT was studied by X-ray measurements at two levels of tube twisting: after 30°, and 240° on the internal surfaces of the tubes. The following estimated shear strains can be obtained from eqs. (14) and (15) for the two cases:  $\gamma \cong 3.9$ , and 32, respectively. The textures are displayed in Fig. 23 in form of {00.2} and {10.0} pole figures. For the lower strain, two cases were examined by increasing the axial stress from 1 GPa to 2 GPa. The initial texture was a characteristic texture of an extruded Mg tube with the basal poles oriented in the radial direction of the tube forming a basal fiber texture. This type of texture in extruded Mg alloys has been reported in Refs. 25, 26).

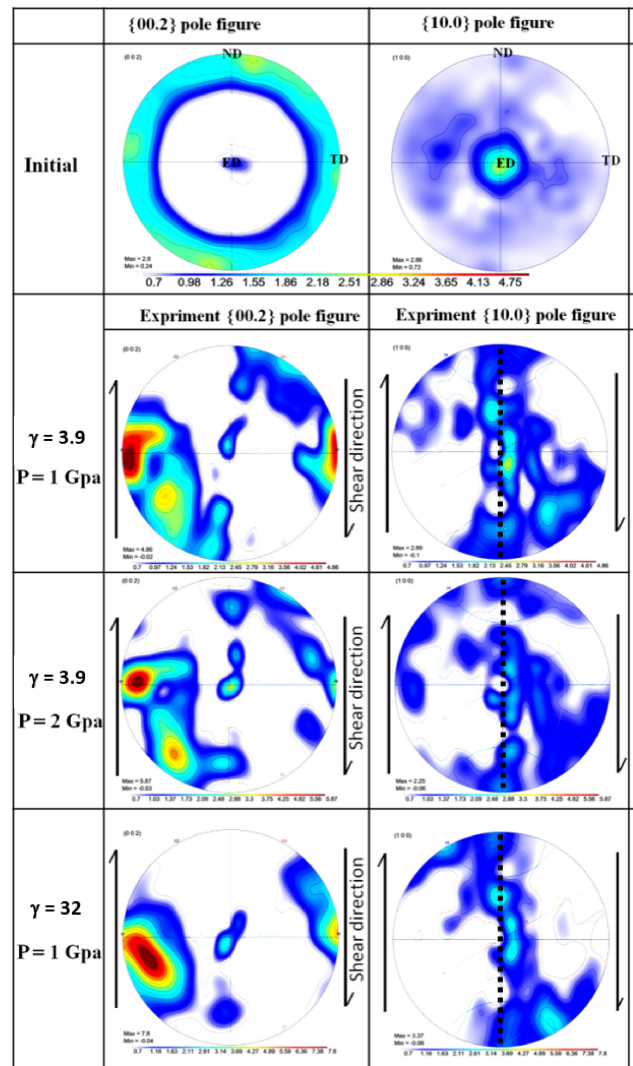


Fig. 23 Crystallographic textures measured by X-ray in Mg sample deformed by HPTT at room temperature. The vertical dotted line shows the position of the main ideal B fiber of hcp simple shear textures in the {10.0} pole figure.

The texture has changed radically after a shear strain of 3.9 with respect to the initial texture (Fig. 23). The main characteristic is the appearance of the B fiber texture: the basal plane nearly parallel to the plane of shear. Nevertheless, there are significant deviations from the exact B fiber: a large population of grain orientations are rotated opposite to the applied shear direction. A main observation is that the texture was about the same at the very large strain, too (at  $\gamma = 32$ ).

Only the intensity was increasing (from the maximum 4.86 to 7.8). The texture is also independent of the applied axial pressure, which is demonstrated in Fig. 23 for the smaller strain ( $\gamma = 3.9$ ).

A general feature of the texture is that the experimental B fiber is rotated with respect to its ideal position; see the vertical dotted line for the exact position of the B fiber in Fig. 23. Such rotation of the texture was also seen in HPT of Mg.<sup>27)</sup> The fiber appears in rotated position, opposite to the applied shear which is suggesting that the grain orientations do not cross the ideal position, not even after a shear strain of 32. Normally the grain orientations should reach the ideal position during large strain and even pass to the other side. This has been shown in Ref. 28) for simple shear of Mg when only slip is the deformation mechanism. The fact that it is not happening in HPTT of Mg means that there is also another micro mechanism. One can suggest the occurrence of dynamic recrystallization (DRX) due to the relatively high temperature (for Mg at room temperature) and also because of the very large strain. This is strongly supported by the observed grain shapes. Indeed, the grains are not elongated as they should be due to the simple shear deformation mode. This effect is partially produced by the grain fragmentation mechanism but continuous DRX can also happen during which the grain boundaries migrate. The net effect is a relatively globular shape of the grains, clearly visible in Figs. 21–22 at large strains. The effect of DRX on the texture evolution is still to be clarified in shear of Mg. Apparently, it produces the tilt of the orientations from the expected ideal orientation, as observed in the present study. The grain fragmentation process is also expected to produce such orientation tilt between the original mother grain and their “daughter-grains”. This can be supported by the grain fragmentation model of Toth *et al.*<sup>29)</sup> in which the lattice curvature produces the fragmentation. The model predicts that the lattice rotation is slower in the grain boundary region of a grain which leads to the build-up of geometrically necessary dislocations and further new grain boundaries. Due to this mechanism, the new grains are necessarily in less advanced positions with respect to the mother grain orientation. So the mother grain can approach the ideal position while the orientation of its fragmented part is retarded. This mechanism can also lead to significant tilts of the experimental texture components with respect to the respective ideal locations and contributes to the observed texture-tilt. Detailed simulation work is needed to verify the above proposed mechanism using the lattice-curvature based grain fragmentation model.

## 9. HPTT of Copper

Well known experimental evidence is that the grain fragmentation process stabilizes at extremely large strains at a given, constant average grain size, see the review paper on this topic by Pippan *et al.*<sup>30)</sup> This stage is a steady state where not only the grain size remains constant but also the flow stress of the material remains unchanged.<sup>31)</sup> The most important parameters influencing the onset of steady state are temperature, alloying and the mode of deformation; cyclic or monotonic.<sup>30)</sup> It has been shown in Ref. 31) that the steady

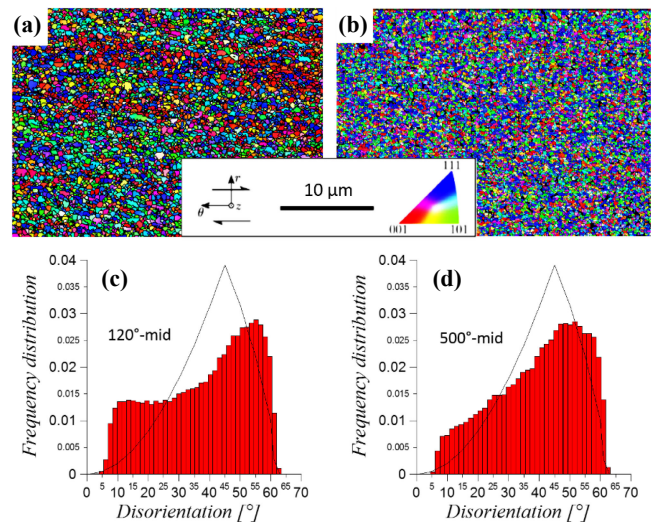


Fig. 24 EBSD-microstructure after an equivalent strain of 16 (a) and 65 (b) observed in pure Cu twisted by HPTT at room temperature. (c) and (d) shows the corresponding next-neighbor disorientation angle distributions.

state stage obtained by SPD techniques is an extension of the so-called Derby relation, which was established for the similar steady state of DRX processes, examined in Refs. 32, 33) for conventional grain sizes. This is a good indication that similar processes are operating in ultra-fine grained materials like in much larger grain sizes during DRX. More direct evidence is the microstructure itself, which shows nearly equiaxed grains instead of elongated ones, which would be expected due to the large plastic strain. An example is shown in Fig. 24, for the case of pure copper, twisted to 120° and 500° by HPTT, corresponding to average von Mises equivalent strains of 16 and 65 within the tubes, taken from the middle area of the tube thickness.<sup>8)</sup> The average grain sizes are 380 nm and 250 nm for these two deformation stages of pure Cu. Therefore, at an equivalent von Mises strain of 16, the material is not yet in the steady state because further grain size reduction is taking place subsequently. The evolution of microstructure between the two strain states can be much appreciated in the disorientation distributions, see Fig. 24(c)–(d). At a strain level of 16, the distribution still displays two maxima, while at the strain of 65, there is only one maximum. At the same time, the distribution approaches more the Mackenzie-type, which belongs to random orientation distribution of neighboring grains. Actually the disorientation distributions of neighboring grains can never be exactly of Mackenzie type, because the crystallographic texture cannot become completely random. For monotonic plastic strain, a particular texture always develops, which is different from a random texture. Particularly, in simple shear deformation of fcc polycrystals, some of the main ideal orientations are 60° away in orientation space, so when such grains are neighbors, they produce extra contribution to the probability density function (the B/ $\bar{B}$  ideal orientations). This is why the distribution overshoots the Mackenzie one near the 60° position in Fig. 24(c) and (d).

## 10. HPTT of IF Steel

The HPTT technique was successfully applied also on

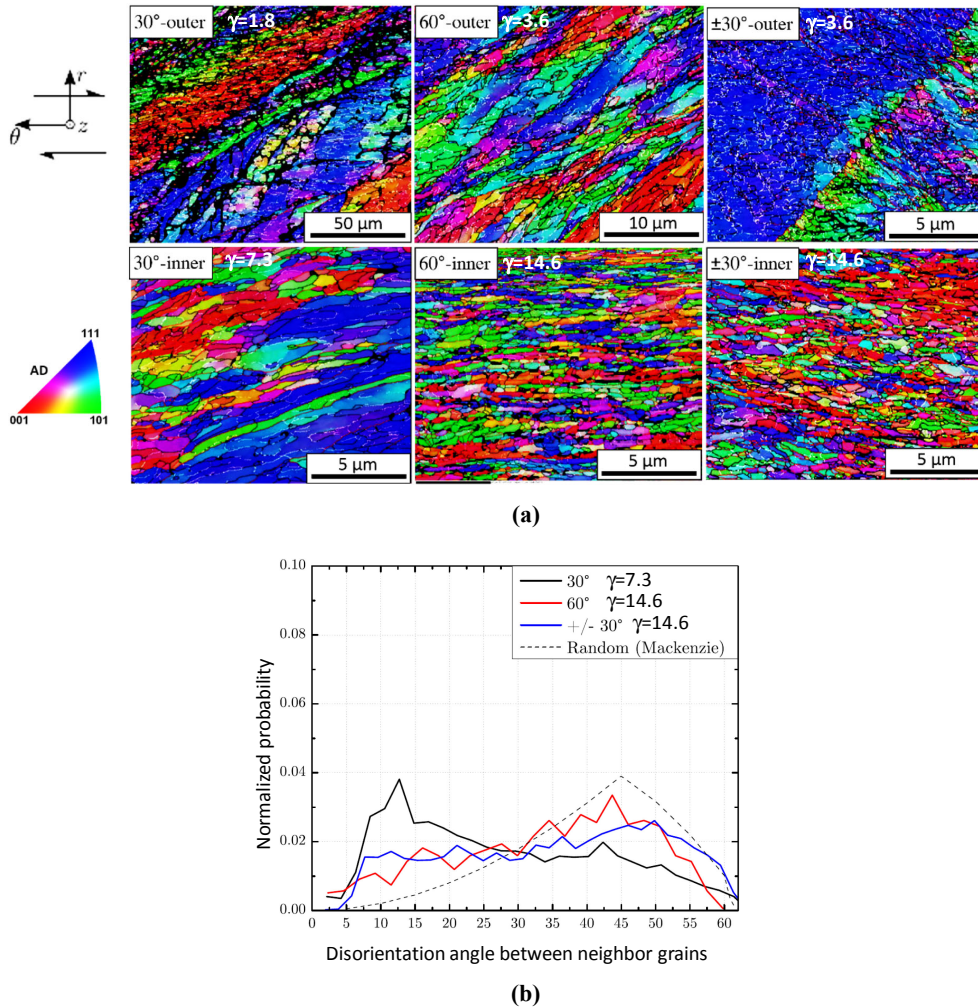


Fig. 25 (a): Microstructure in IF steel tube twisted in HPTT by 30°, 60°, and  $\pm 30^\circ$  obtained by EBSD. (b): The grain-to-grain disorientation angle distribution for large strains. The indicated shear strain values were obtained by the empirical relation (eq. (14)) with  $n = 2$ ,  $m = 20$ . Data are from Ref. 8.

relatively hard metals, such as IF steel.<sup>8)</sup> Figure 25 presents the microstructural evolution at 30° and 60° twisting and also for reversed strain: first +30°, followed by -30° rotation, both at the external and internal surfaces of the tube. There are four microstructures in Fig. 25 for monotonically increasing shear strain; these were recorded at shear strains of 1.8, 3.6, 7.3 and 14.6. (These shear strains were estimated using the empirical formula given in eq. (14).) By taking into account the unit scale on the corresponding microstructures, it is clear that a very efficient grain fragmentation took place; the initial grain boundaries became rapidly non-traceable with the appearance of new high angle grain boundaries. Although at a shear strain of 14.6 the grains show some elongation in the direction of shear, however, with aspect ratios lesser than expected without grain subdivision.

The grain-to-grain disorientation angle distribution is displayed in Fig. 25(b) for a shear strain of 7.3. As can be seen, the shear strain of 7.3 is not yet enough to approach the random distribution, but at the shear strain of 14.6, the measured curve is much closer to the Mackenzie plot. Perfect coincidence is not expected because it is possible only if the crystallographic texture is random. However as mentioned earlier (Section 9), there is always a texture during plastic deformation and it has significant effect on the disorientation

distribution. Therefore, the Mackenzie distribution cannot be perfectly obtained by severe plastic deformation.

It is interesting to examine the evolution of the microstructure when the shear direction is inverted by the same amount as the forward one, so that the accumulated absolute value of shear strain is the same as that for the monotonic case. As depicted in Fig. 25(a), for low strains, the initial grain boundaries are nearly reconstructed after strain reversal. This is not the case, however, for large strains (see in Fig. 25(a) in the right lower corner). In fact, the microstructure seems quite similar to the monotonic one, even the disorientation angle distribution is nearly the same (see in Fig. 25(b)). This suggests that the grain fragmentation process is not reversible after a sufficiently large amount of strain; the material 'loses its memory' for the grain shape if the fragmentation is very much advanced. The critical amount of monotonic strain for this effect must be larger than the shear strain of 1.8; it is estimated to be situated in the interval of about  $\gamma = 3,6-7,3$ .

The evolution of the average grain size as a function of strain is shown in Fig. 26 (the grain size is defined as the diameter of a circle of the same surface as the grain). There is a continuous decrease, which is composed of two stages. In the first stage, there is a rapid decrease up to about a shear

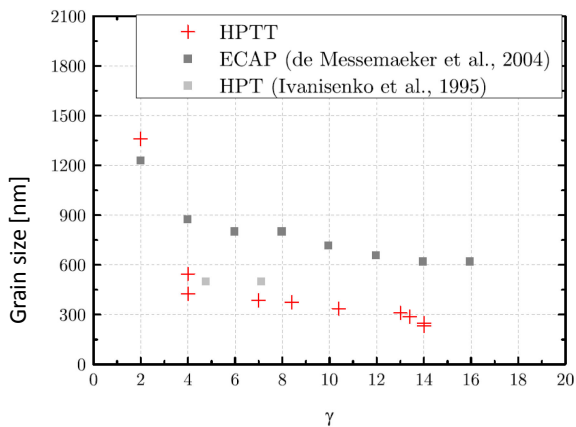


Fig. 26 Grain size variation during HPTT of IF steel (red crosses). For comparison, the grain sizes obtained by ECAP and HPT are also plotted. Data are from Refs. 8, 25, 27.

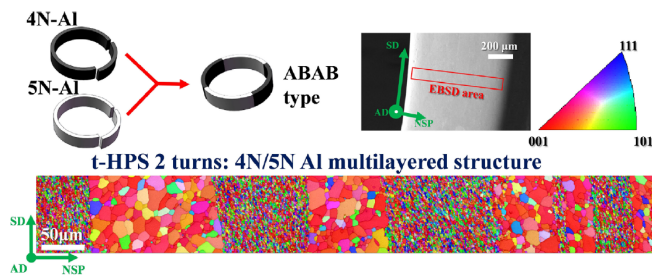


Fig. 27 Multilayered structure fabricated by HPTT of a tube composed of two Al alloys; 5N and 4N purity, after two turns at room temperature<sup>11)</sup> (reproduced by permission).

strain of 4, from which another stage starts with a much smaller slope. At the largest strain, the grain size is only about 230 nm. For comparison, the grain sizes obtained by other SPD techniques are also plotted in Fig. 27. It is interesting to note that—except for the low strain region—ECAP of IF steel produces twice larger grain sizes,<sup>34)</sup> while the HPT of this material leads to a comparable grain size.<sup>35)</sup> The explanation for the difference in grain refinement for ECAP could be related to the presence of high hydrostatic stresses in both HPT and HPTT. High hydrostatic stresses are needed because in both of these techniques, the deformation is achieved by friction. Such high hydrostatic stress, however, is not needed in ECAP because the material is pushed through the die directly, the friction just hinders the process. The application of a back pressure increases the hydrostatic pressure in ECAP; indeed, it is lowering the grain size.<sup>36)</sup> The smaller grain sizes under high hydrostatic pressure can be attributed to the higher activation energy of vacancies.<sup>37,38)</sup> These point defects are sensitive to the added hydrostatic stresses due to their own generated hydrostatic stress, so the addition of a compressive stress increases the energy necessary for their diffusion. The point defects are important in the dislocation annihilation processes; their reduced mobility leads to higher dislocation densities, so more dislocations are available to produce polarized dislocation walls which form the basis of the grain fragmentation process.

## 11. Architecturing a Tube by HPTT

The most well-known technique to produce architected metal is accumulated roll bonding (ARB). In ARB, two different metals are rolled together by successive SPD operations producing multilayered composite materials with interesting properties.<sup>39)</sup> HPTT is also suitable for producing architected material in tube form. Li *et al.*<sup>11)</sup> presented experimental studies and a theoretical analysis for synthesizing multilayered laminates from lead and tin and also from two kinds of pure aluminum: 4NAl and 5NAl. The experimental procedure for the 4NAl–5NAl case is presented in Fig. 27. The initial tube was composed of four equal size parts; two of them were 4N and the other two were from 5N Al. After two HPTT turns, 8 layers were formed with alternating microstructures. The geometry of the boundary layers could be described with the help of the trace-line equation which could be obtained from the strain gradient equation.

In the experiments, the 4N layers showed much smaller grain size with little elongation in the shear direction, while the 5N layers were composed of equiaxed recrystallized grains (Fig. 27). This experiment is also a good example for showing the occurrence of dynamic recrystallization at large strains in SPD processes which leads to equiaxed grains in the UFG domain. There was perfect bonding between the different layers which was attributed to the extreme increase in the contact area between adjacent materials. A very strong point of obtaining multilayered structures by HPTT in contrast to ARB is that it is possible to do it in a single HPTT operation while many elaborate passes are needed in ARB for a similar result.

## 12. Summary

The present review provides various aspects of the HPTT processing technique with many examples. The main results of the papers written on HPTT ever since the process was introduced (2009) have been presented and discussed. New results have also been added, which are the outcome of two recent Ph.D. theses (Chen Cai 2016, Arnaud Pougis 2012).

Special attention has been paid to the strain gradient that always appears within the tube wall. For the purpose of practical estimations of the strain in different parts of the tube, an empirical function containing only two parameters has been proposed in the present work. It has been shown that the strain gradient depends linearly on the amount of twisting.

Selected experimental results pertaining to HPTT of aluminum (pure, commercially pure and alloyed), copper, magnesium, and IF steel have been presented and discussed in the light of microstructural evolution during HPTT. The microstructural studies have been carried out using optical microscopy, and scanning electron microscopy involving orientation imaging by electron back-scatter diffraction (EBSD) and transmission Kikuchi diffraction (TKD). The mechanical strength has been evaluated directly from the torque measured during the process.

The detailed analysis of grain fragmentation process during HPTT has revealed that HPTT is effective as HPT,

and is more effective than the other SPD processes. For example, the grain size after HPTT is about half the grain size obtained after ECAP for IF steel.

The disorientation angle distribution between neighboring grains has been found to evolve with strain from a single peak (at low angles) at lower strains to a double peak at larger strains and finally again to a single peak (at large angles) in the steady state of grain fragmentation. The evolution of the disorientation distribution can also be used for the estimation of the strain, if it is not known otherwise.

The texture evolution in HPTT corresponds to simple shear textures. HPTT is a very suitable process to study shear textures up to extremely large strains. The texture weakens at extreme large strains but does not become random. The presence of texture leads to deviation from ideal Mackenzie-type distribution in the measured disorientation angle distributions, even in the steady state.

The results obtained for the study of microstructure, texture and strength concur with the generally observed basic phenomena observed in SPD processes in the case of HPTT. For example, the occurrence of a strong grain fragmentation process which leads to an equiaxed grain structure in the steady state through the simultaneous effects of grain fragmentation and grain boundary migration by stress induced dynamic recrystallization.

The overall analyses of results clearly indicate that the HPTT process can be considered as an efficient SPD technique to manufacture high strength metallic tubes with UFG structures.

## Acknowledgements

The authors acknowledge the financial help received from the French ANR project called 'Hypertube'. The work was also supported by the National Research Agency, France referenced as ANR-11-LABX-008-01 (LabEx DAMAS).

## REFERENCES

- 1) L.S. Toth, M. Arzaghi, J.J. Fundenberger, B. Beausir, O. Bouaziz and R. Arruffat-Massion: *Scr. Mater.* **60** (2009) 175–177.
- 2) R.Z. Valiev and T.G. Langdon: *Prog. Mater. Sci.* **51** (2006) 881–981.
- 3) A. Zhilyaev and T. Langdon: *Prog. Mater. Sci.* **53** (2008) 893–979.
- 4) M. Arzaghi, J.J. Fundenberger, L.S. Toth, R. Arruffat, L. Faure, B. Beausir and X. Sauvage: *Acta Mater.* **60** (2012) 4393–4408.
- 5) J.T. Wang, Z. Li, J. Wang and T.G. Langdon: *Scr. Mater.* **67** (2012) 810–813.
- 6) A. Pougis, L.S. Toth, O. Bouaziz, J.-J. Fundenberger, D. Barbier and R. Arruffat: *Scr. Mater.* **66** (2012) 773–776.
- 7) M. Arzaghi: Ph.D. Thesis, Paul Verlain University, (2010).
- 8) A. Pougis: Ph.D. Thesis, Lorraine University, (2013).
- 9) C. Chen: Ph.D. Thesis, Lorraine University, (2016).
- 10) G.R. Canova, U.F. Kocks and J.J. Jonas: *Acta Mater.* **32** (1984) 211–226.
- 11) Z. Li, P.F. Zhang, H. Yuan, K. Lin, Y. Liu, D.L. Yin, J.T. Wang and T.G. Langdon: *Mater. Sci. Eng. A* **658** (2016) 367–375.
- 12) M. Zehetbauer and V. Seumer: *Acta Metall. Mater.* **41** (1993) 577–588.
- 13) Q. Wei, S. Cheng, K.T. Ramesh and E. Ma: *Mater. Sci. Eng. A* **381** (2004) 71–79.
- 14) B. Beausir and J.J. Fundenberger: ATOM - Analysis Tools for Orientation Maps, Lorraine University - Metz, <http://atom-software.eu/> (2015).
- 15) J.-J. Fundenberger and B. Beausir: JTEX - Software for Texture Analysis Lorraine University - Metz, <http://jtex-software.eu/> (2015).
- 16) L.S. Tóth, B. Beausir, C.F. Gu, Y. Estrin, N. Scheerbaum and C.H.J. Davies: *Acta Mater.* **58** (2010) 6706–6716.
- 17) A.R. Zhilyaev, D.L. Swisher, K. Oh-ishi, T.G. Langdon and T.R. McNelley: *Mater. Sci. Eng. A* **429** (2006) 137–148.
- 18) M. Kawasaki, Z. Horita and T.G. Langdon: *Mater. Sci. Eng. A* **524** (2009) 143–150.
- 19) A.P. Zhilyaev, K. Oh-ishi, G.I. Raab and T.R. McNelley: *Mater. Sci. Eng. A* **441** (2006) 245–252.
- 20) A.P. Zhilyaev, K. Oh-ishi, T.G. Langdon and T.R. McNelley: *Mater. Sci. Eng. A* **410–411** (2005) 277–280.
- 21) Y. Ito and Z. Horita: *Mater. Sci. Eng. A* **503** (2009) 32–36.
- 22) C. Chen, Y. Beygelzimer, L.S. Toth and J.-J. Fundenberger: *Mater. Lett.* **159** (2015) 253–256.
- 23) H. Yuan, E. Brodu, C. Chen, E. Bouzy, J.-J. Fundenberger and L.S. Toth: *J. Microsc.* **267** (2017) 70–80.
- 24) S. Biswas, S.S. Dhinwal and S. Suwas: *Acta Mater.* **58** (2010) 3247–3261.
- 25) Y. Huang, R.B. Figueiredo, T. Baudin, A.-L. Helbert, F. Brisset and T.G. Langdon: *Mater. Res.* **16** (2013) 577–585.
- 26) X.G. Qiao, Y.W. Zhao, W.M. Gan, Y. Chen, M.Y. Zheng, K. Wu, N. Gao and M.J. Starink: *Mater. Sci. Eng. A* **619** (2014) 95–106.
- 27) B.J. Bonarski, E. Schafler, B. Mingler, W. Skrotzki and B. Mikulowski: *J. Mater. Sci.* **43** (2008) 7513–7518.
- 28) B. Beausir, L.S. Toth and K.W. Neale: *Acta Mater.* **55** (2007) 2695–2705.
- 29) L.S. Tóth, Y. Estrin, R. Lapovok and C. Gu: *Acta Mater.* **58** (2010) 1782–1794.
- 30) R. Pippin, F. Wetscher, M. Hafok, A. Vorhauer and I. Sabirov: *Adv. Eng. Mater.* **8** (2006) 1046–1056.
- 31) A. Pougis, L.S. Toth, J.J. Fundenberger and A. Borbely: *Scr. Mater.* **72–73** (2014) 59–62.
- 32) B. Derby: *Acta Mater.* **39** (1991) 955–962.
- 33) B. Derby: *Scr. Mater.* **27** (1992) 1581–1585.
- 34) J. De Messemaeker, B. Verlinden and J. Van Humbeeck: *Mater. Lett.* **58** (2004) 3782–3786.
- 35) Y.V. Ivanisenko, A.V. Korznikov, I.M. Safarov and R.Z. Valiev: *Nanostruct. Mater.* **6** (1995) 433–436.
- 36) P.W.J. Mckenzie, R. Lapovok and Y. Estrin: *Acta Mater.* **55** (2007) 2985–2993.
- 37) E. Schafler: *Scr. Mater.* **64** (2011) 130–132.
- 38) E. Schafler: *Scr. Mater.* **62** (2010) 423–426.
- 39) Y. Saito, N. Tsuji, H. Utsunomiya, T. Sakai and R.G. Hong: *Scr. Mater.* **39** (1998) 1221–1227.